Optimizing Ligand Structure for Low-Loading and Fast Catalysis for Alkynyl-Alcohol and -Amine Cyclization

Supporting Information

*James M. Stubbs, Benjamin J. Bridge, and Johanna M. Blacquiere**
Department of Chemistry
University of Western Ontario
London, Ontario, Canada, N6A 5B7

Table of Contents

I – NMR Spectra

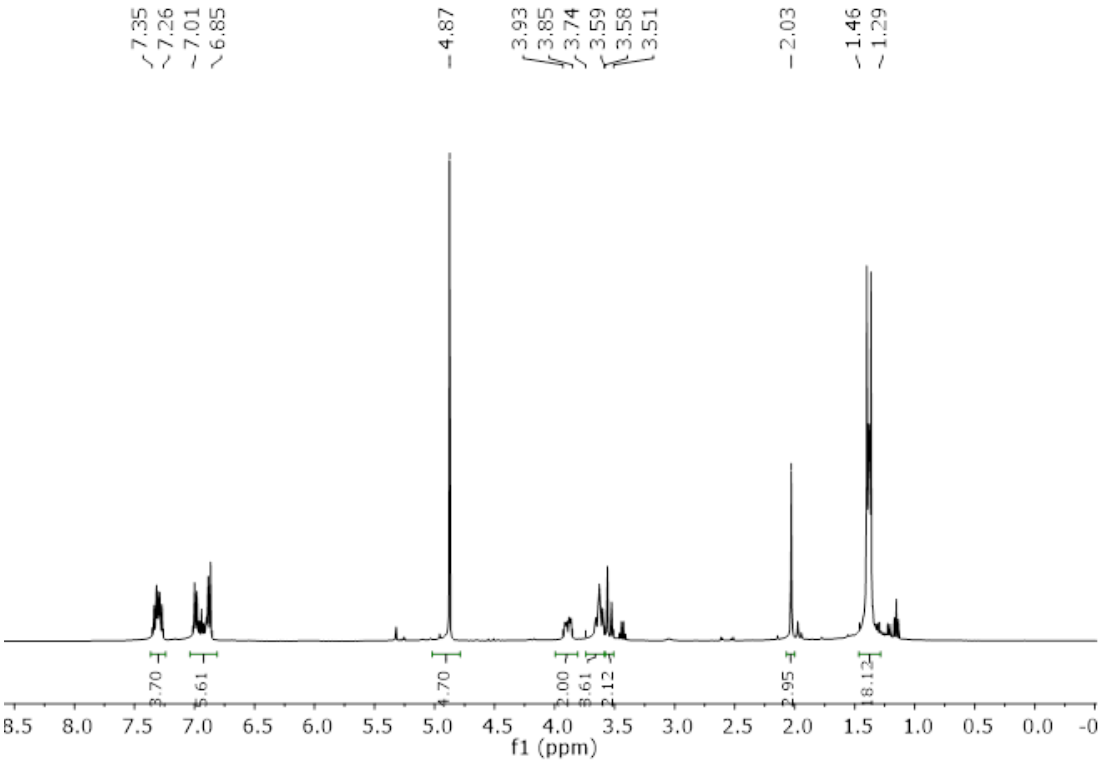

Figure S1. ^{1}H NMR spectrum of [Ru(Cp)($P^{tBu}_2N^{Ph}_2$)(MeCN)]PF_6 (**1d**) in CD_2Cl_2.

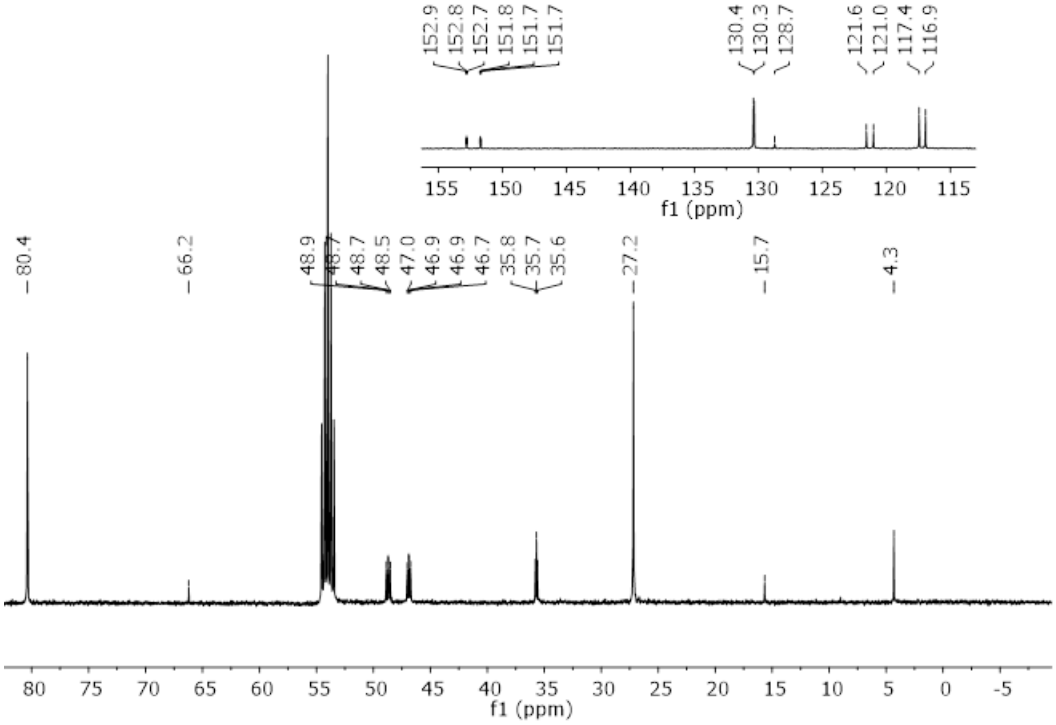

Figure S2. $^{13}C\{^{1}H\}$ NMR spectrum of [Ru(Cp)($P^{tBu}_2N^{Ph}_2$)(MeCN)]PF_6 (**1d**) in CD_2Cl_2.

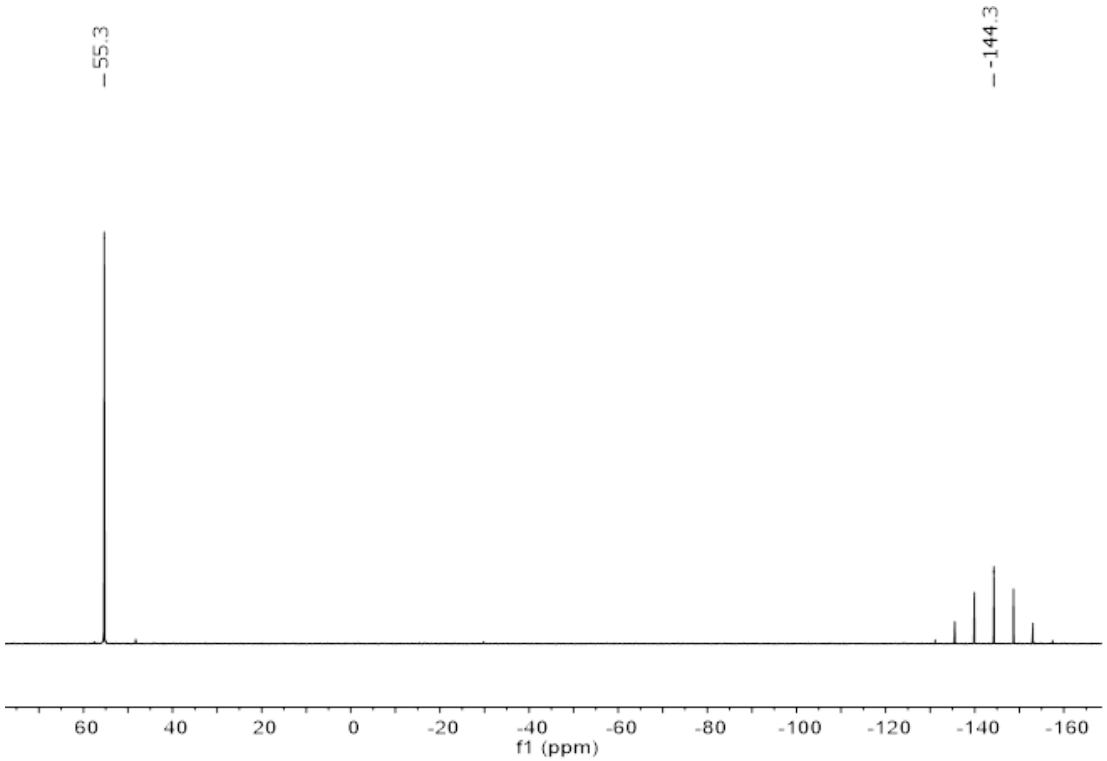

Figure S3. $^{31}P\{^{1}H\}$ NMR spectrum of [Ru(Cp)($P^{tBu}{}_2N^{Ph}{}_2$)(MeCN)]PF_6 (**1d**) in CD_2Cl_2.

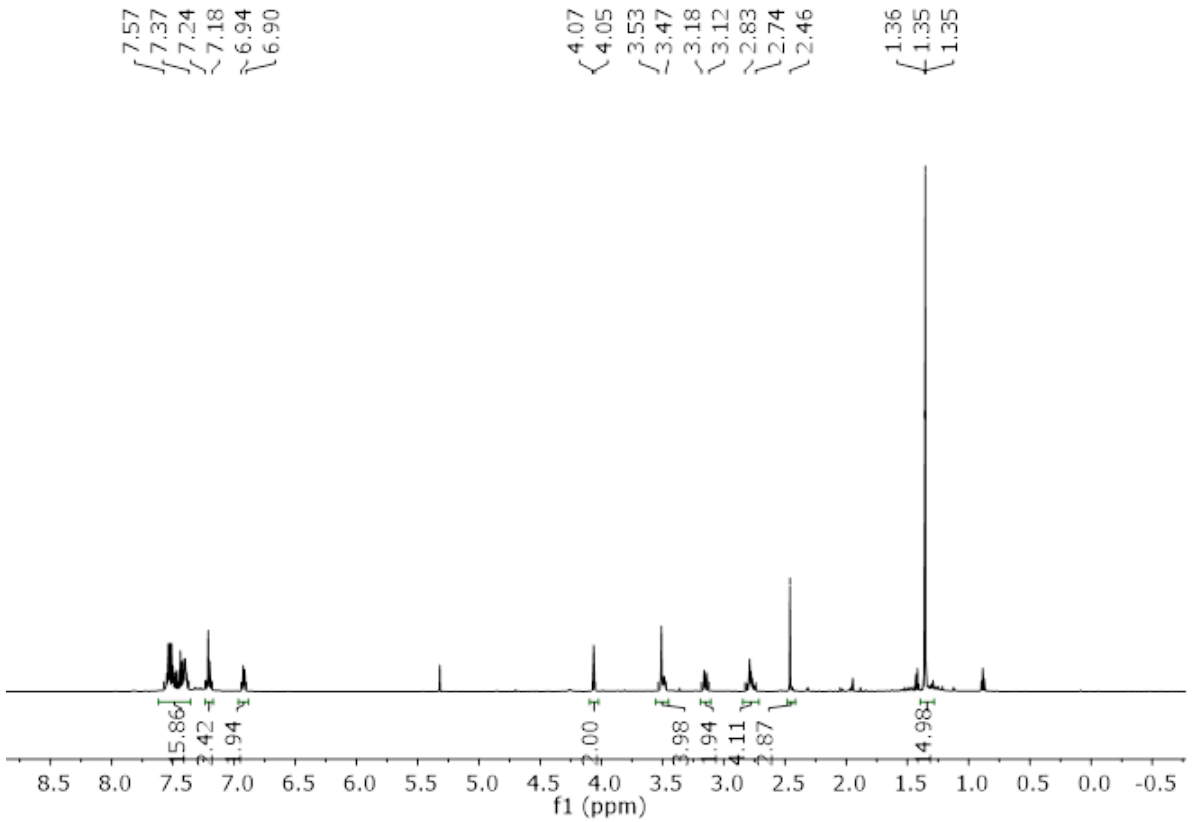

Figure S4. ^{1}H NMR spectrum of [Ru(Cp*)($P^{Ph}{}_2N^{Bn}{}_2$)(MeCN)]PF_6 (**2a**) in CD_2Cl_2.

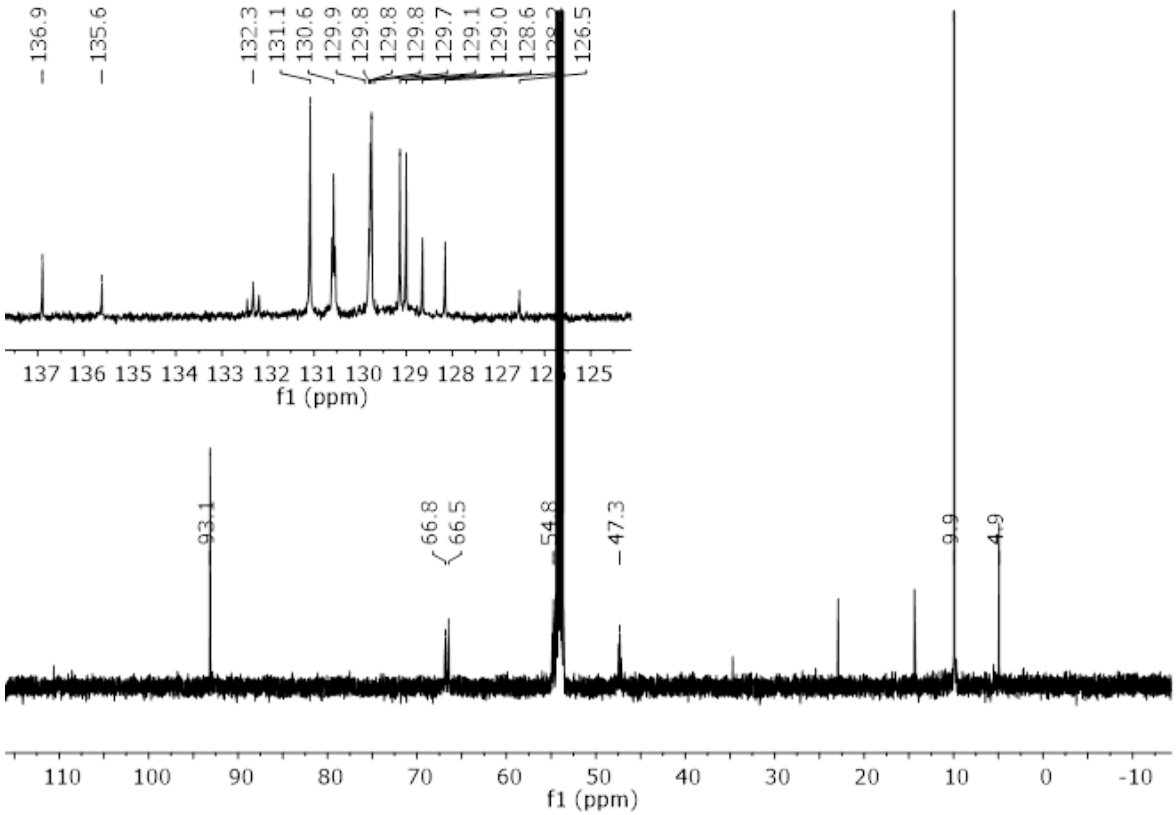

Figure S5. $^{13}C\{^{1}H\}$ NMR spectrum of [Ru(Cp*)($P^{Ph}_2N^{Bn}_2$)(MeCN)]PF_6 (**2a**) in CD_2Cl_2.

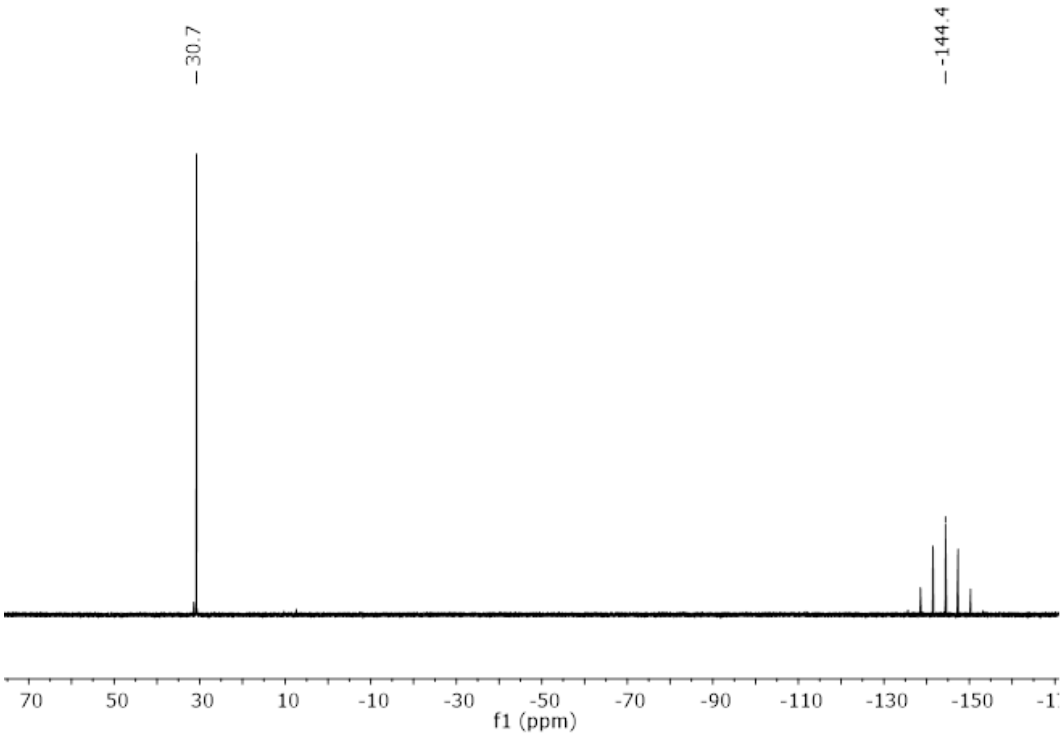

Figure S6. $^{31}P\{^{1}H\}$ NMR spectrum of [Ru(Cp*)($P^{Ph}_2N^{Bn}_2$)(MeCN)]PF_6 (**2a**) in CD_2Cl_2.

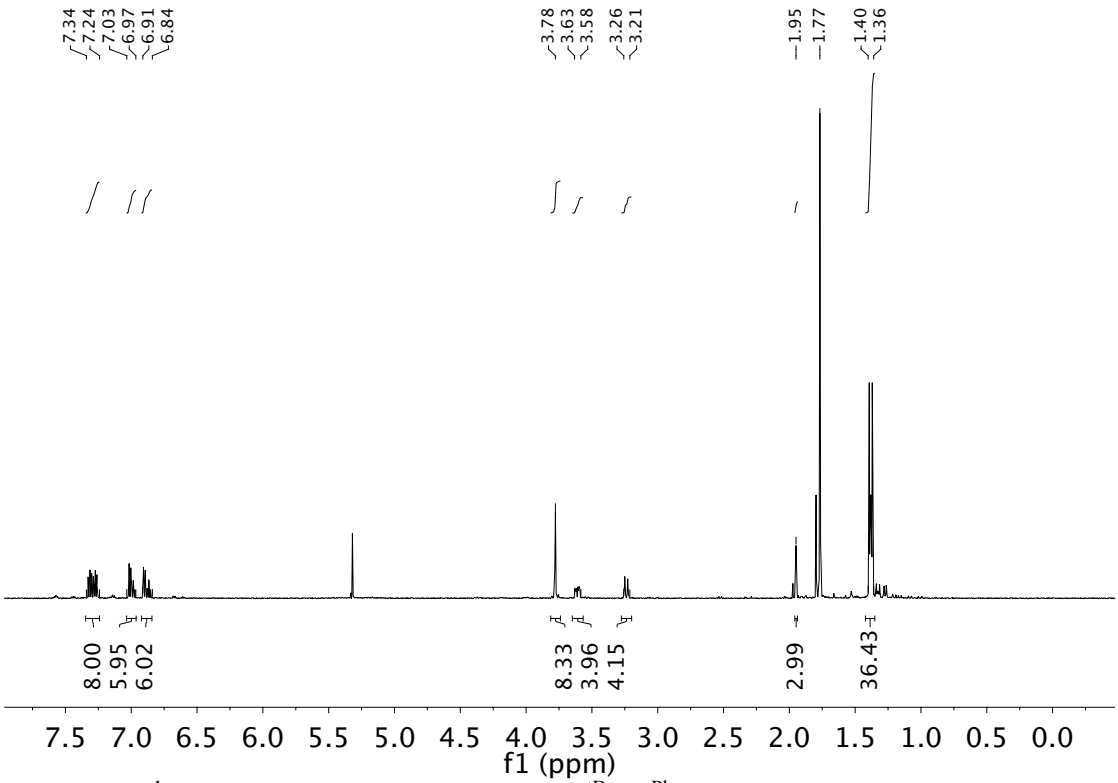

Figure S7. ^{1}H NMR spectrum of [Ru(Cp*)($P^{tBu}_2N^{Ph}_2$)(MeCN)]PF_6 (**2d**) in CD_2Cl_2.

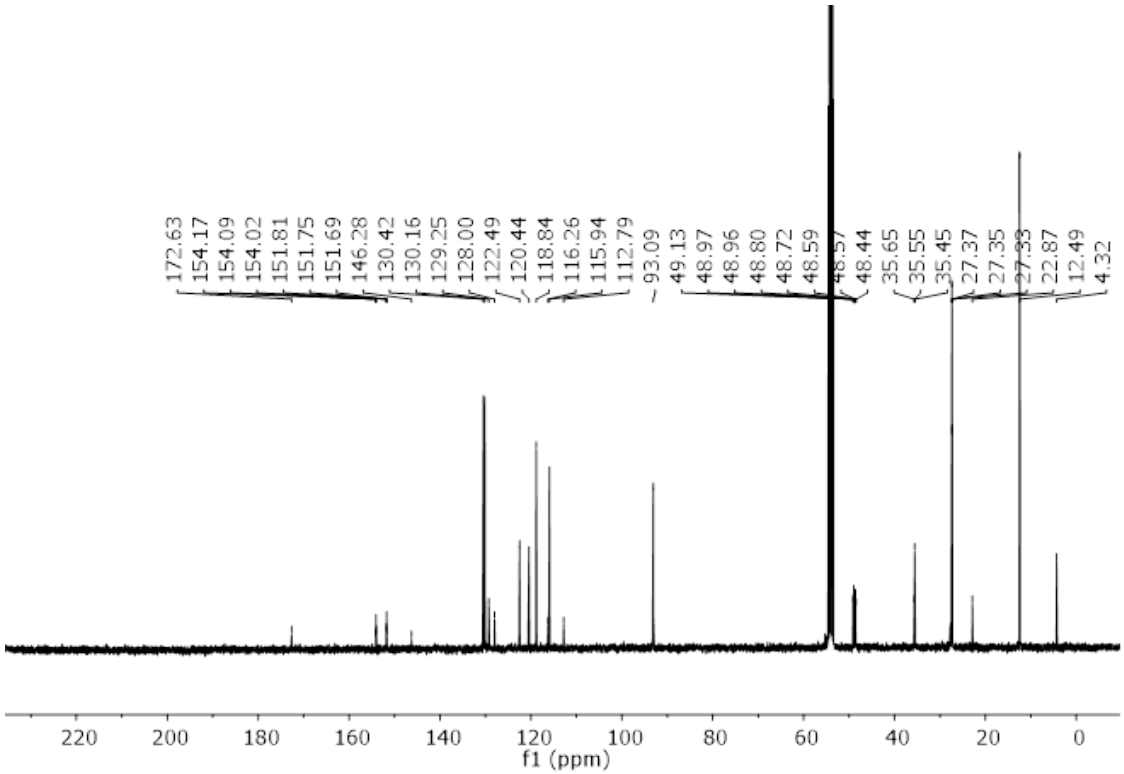

Figure S8. $^{13}C\{^{1}H\}$ NMR spectrum of [Ru(Cp*)($P^{tBu}_2N^{Ph}_2$)(MeCN)]PF_6 (**2d**) in CD_2Cl_2.

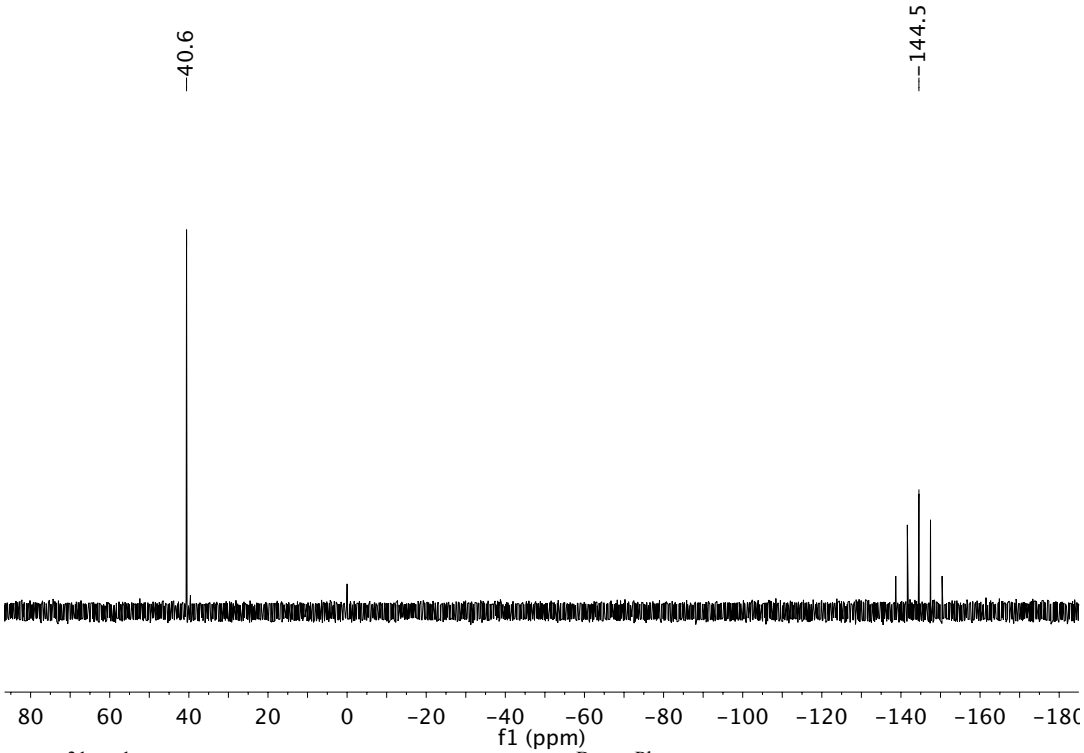

Figure S9. $^{31}P\{^{1}H\}$ NMR spectrum of [Ru(Cp*)($P^{tBu}_2N^{Ph}_2$)(NCMe)]PF_6 (**2d**) in CD_2Cl_2.

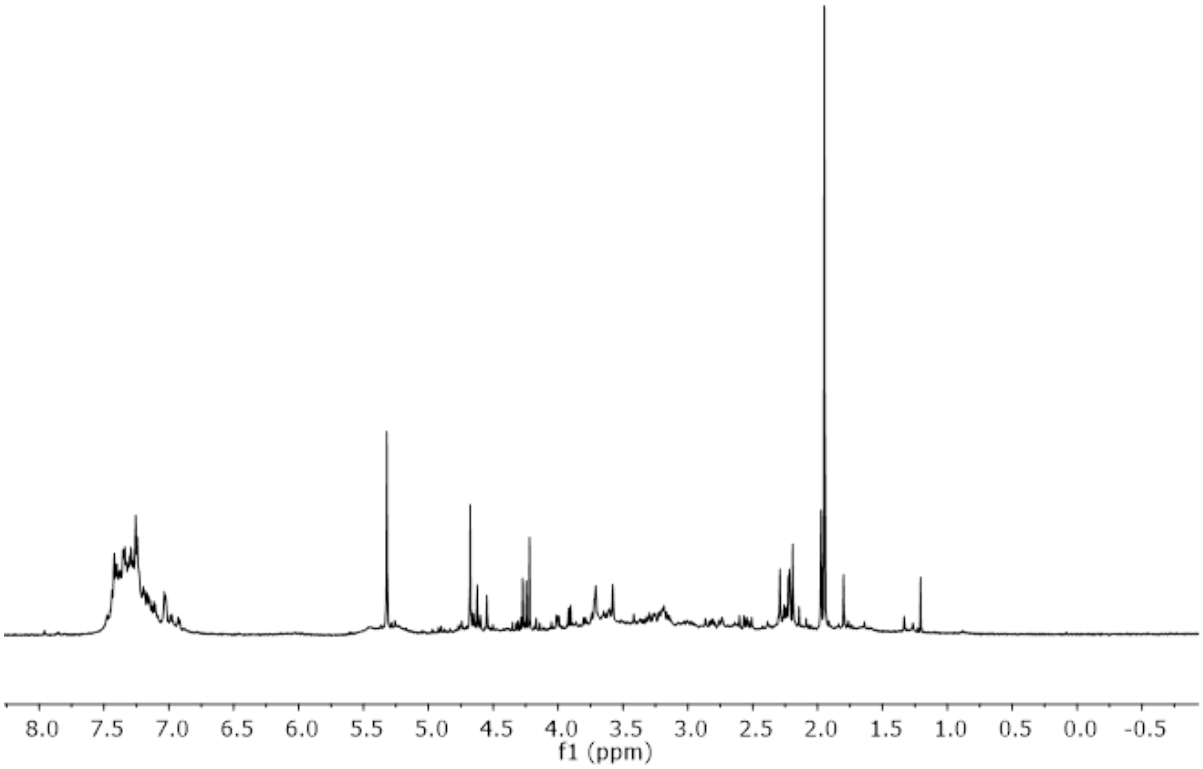

Figure S10. ^{1}H NMR spectrum of [Ru(Cp)($P^{Bn}_2N^{Bn}_2$)(MeCN)]PF_6 (**1c**) in CD_2Cl_2.

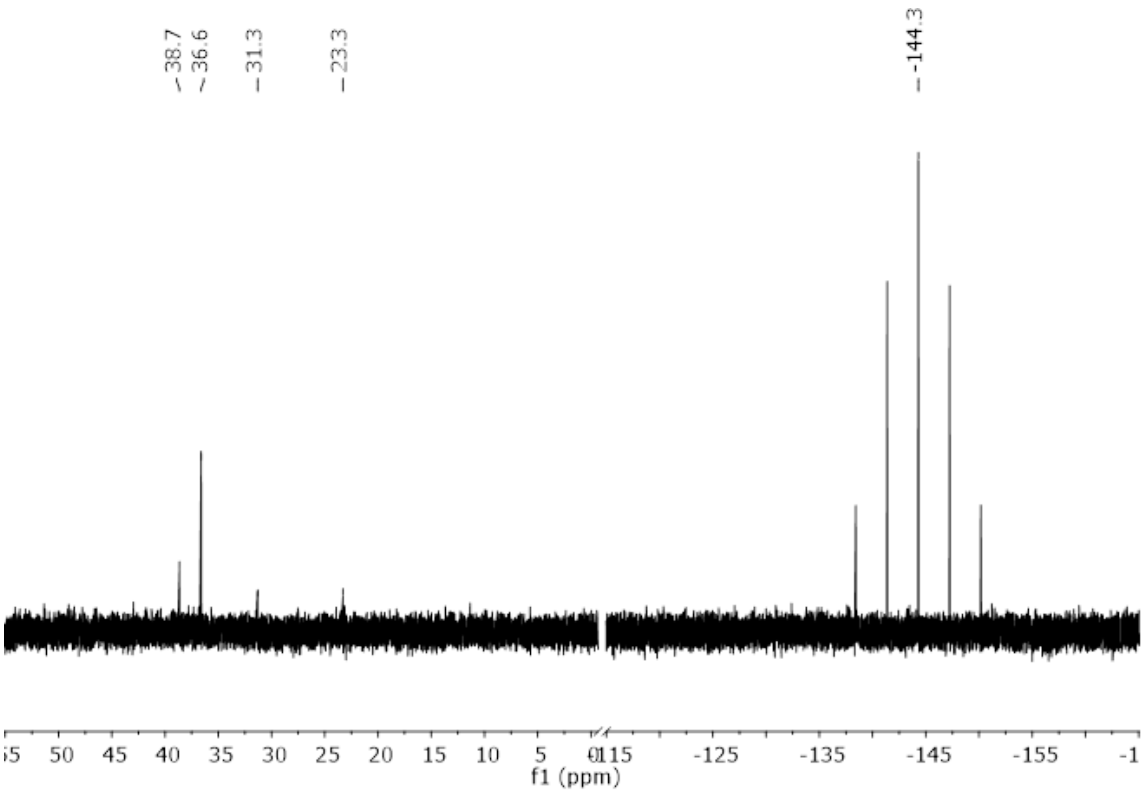

Figure S11. $^{31}P\{^{1}H\}$ NMR spectrum of [Ru(Cp)($P^{Bn}_2N^{Bn}_2$)(MeCN)]PF_6 (**1c**) in CD_2Cl_2.

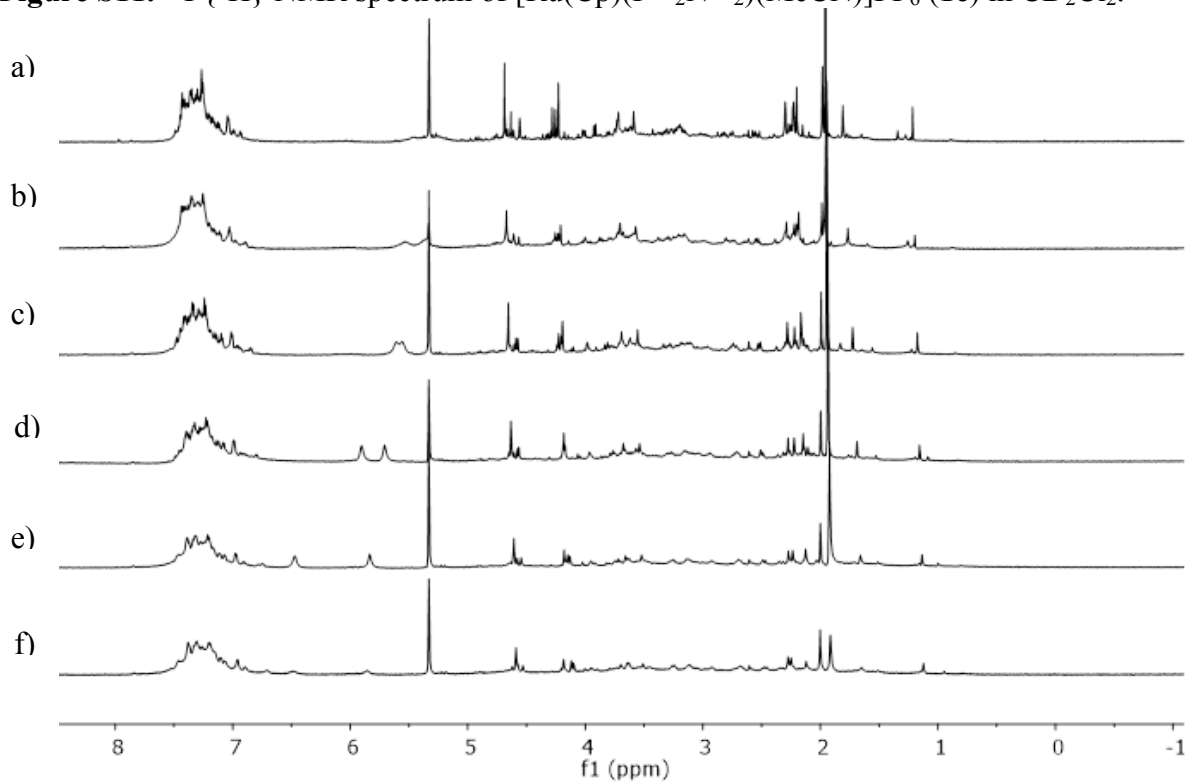

Figure S12. ^{1}H NMR stack plot of [Ru(Cp)($P^{Bn}_2N^{Bn}_2$)(MeCN)]PF_6 (**1c**) in CD_2Cl_2 at: a) 25 °C; b) 0 °C; c) – 25 °C; d) – 50 °C; e) – 75 °C; and f) – 90 °C.

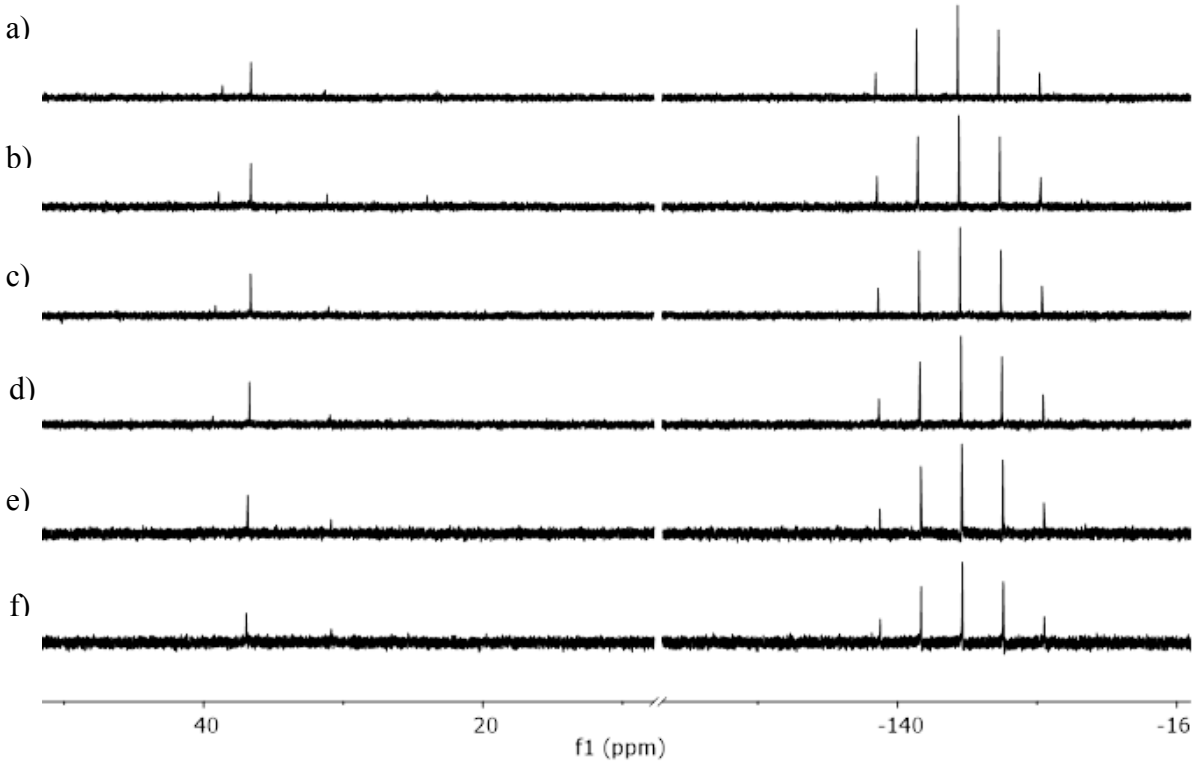

Figure S13. $^{31}P\{^{1}H\}$ NMR stack plot of [Ru(Cp)($P^{Bn}_2N^{Bn}_2$)(MeCN)]PF_6 (**1c**) in CD_2Cl_2 at: a) 25 °C; b) 0 °C; c) – 25 °C; d) – 50 °C; e) – 75 °C; and f) – 90 °C.

II – IR Spectra

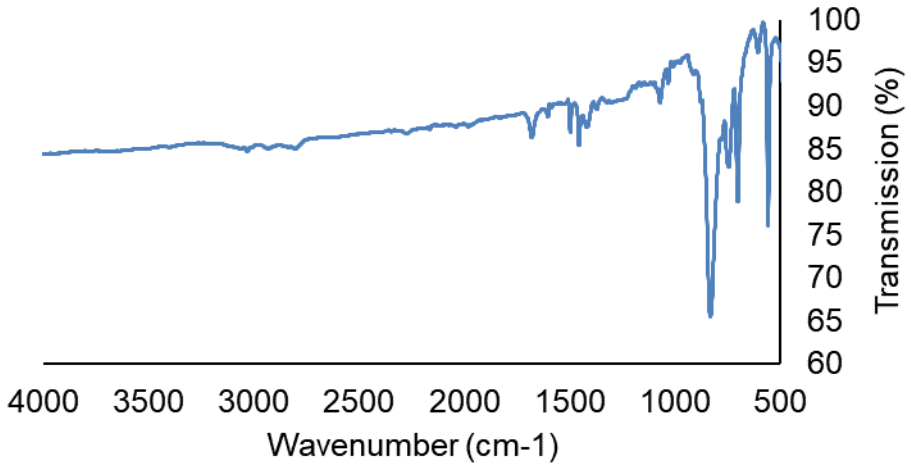

Figure S14. An ATR-FTIR spectrum of solid [Ru(Cp)($P^{Bn}_2N^{Bn}_2$)(NCMe)]PF_6 (**1c**) collected with a PerkinElmer UATR Two FT-IR Spectrum Two.

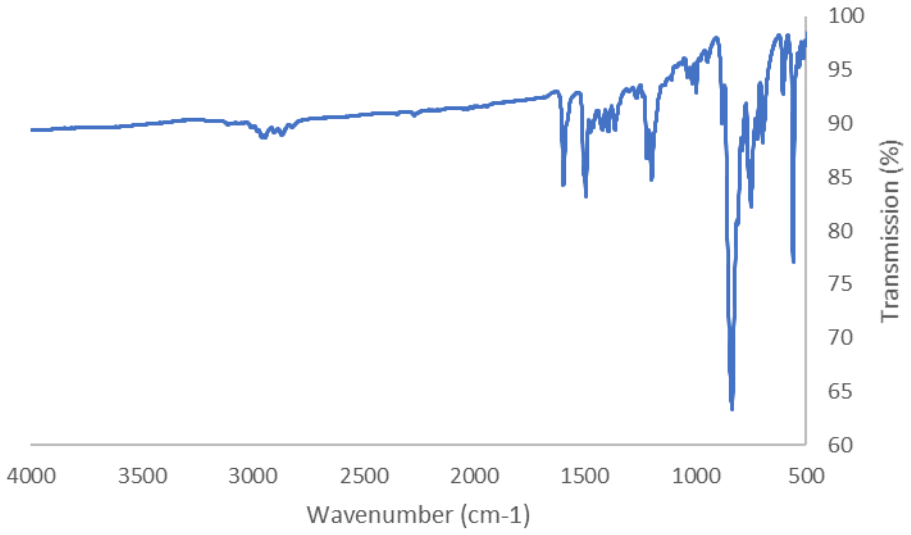

Figure S15. An ATR-FTIR spectrum of solid [Ru(Cp)($P^{tBu}_2N^{Ph}_2$)(NCMe)]PF_6 (**1d**) collected with a PerkinElmer UATR Two FT-IR Spectrum Two.

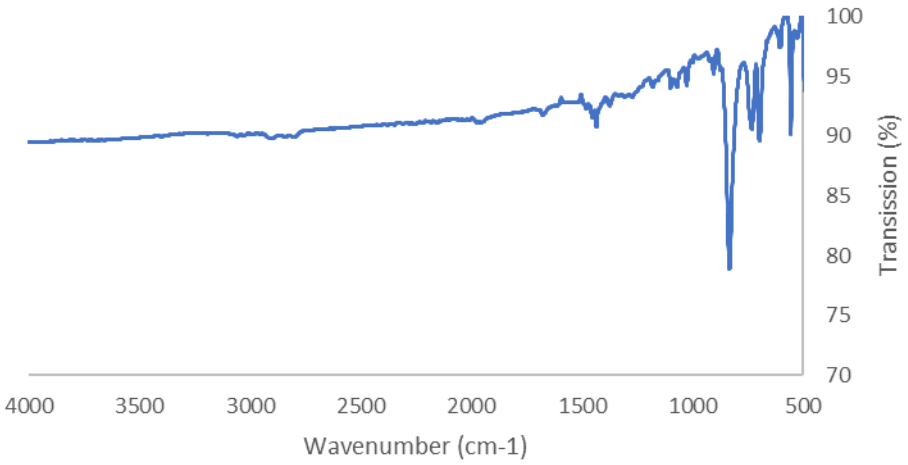

Figure S16. An ATR-FTIR spectrum of solid [Ru(Cp*)($P^{Ph}_2N^{Bn}_2$)(NCMe)]PF_6 (**2a**) collected with a PerkinElmer UATR Two FT-IR Spectrum Two.

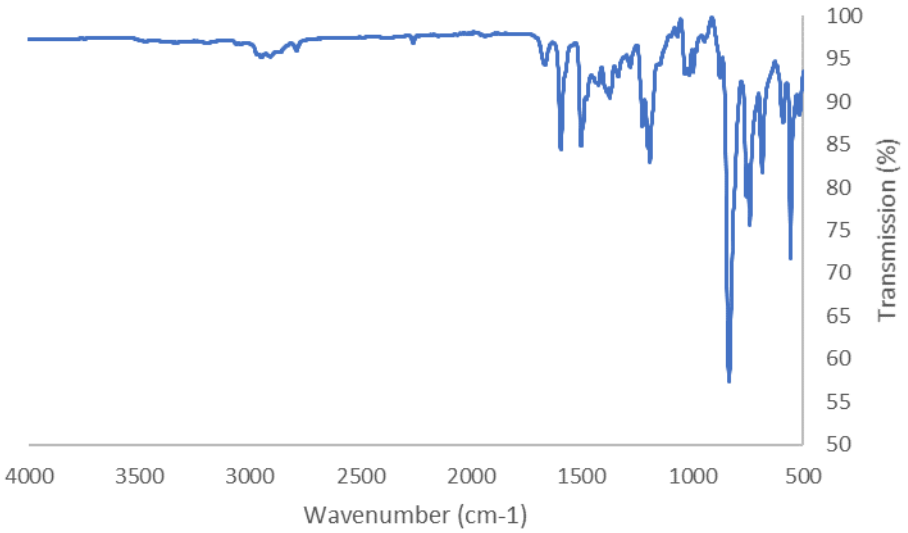

Figure S17. An ATR-FTIR spectrum of solid [Ru(Cp*)($P^{tBu}_2N^{Ph}_2$)(NCMe)]PF_6 (**2d**) collected with a PerkinElmer UATR Two FT-IR Spectrum Two.

III – MALDI Mass Spectrometry Data

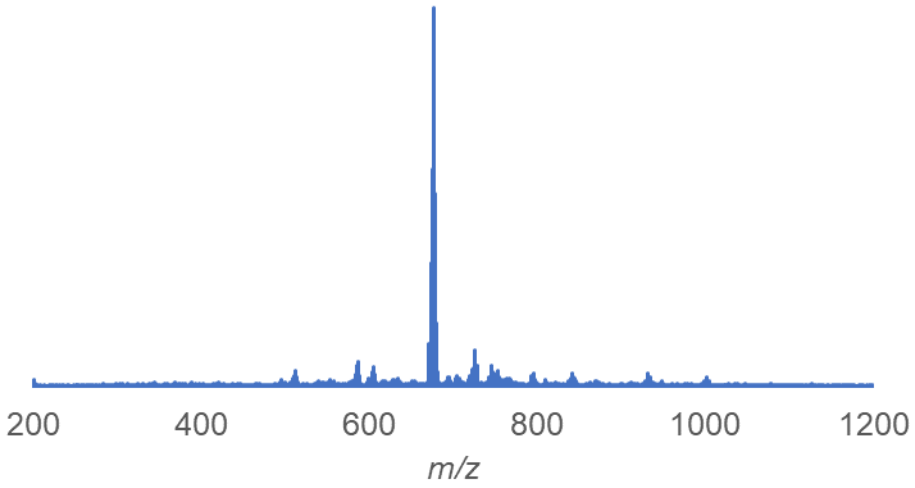

Figure S18. MALDI-TOF mass spectrum of [Ru(Cp)($P^{Bn}_2N^{Bn}_2$)(MeCN)]PF_6 (**1c**) with pyrene as the matrix (1:20 ratio).

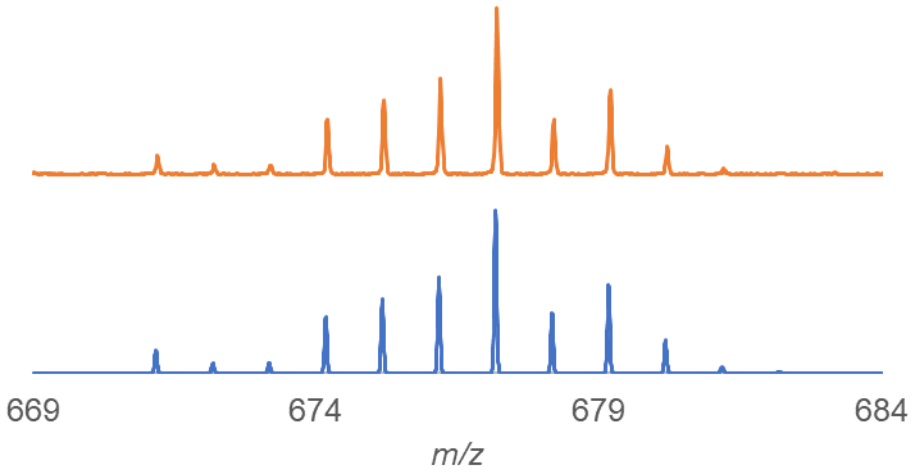

Figure S19. Zoom-in (top) of the observed signal with *m/z* = 677.2 in the MALDI-TOF mass spectrum of [Ru(Cp)($P^{Bn}_2N^{Bn}_2$)(MeCN)]PF_6 (**1c**); and simulation[1] (bottom) of the isotope pattern for the fragment cation [Ru(Cp)($P^{Bn}_2N^{Bn}_2$)]$^+$ with *m/z* = 677.2.

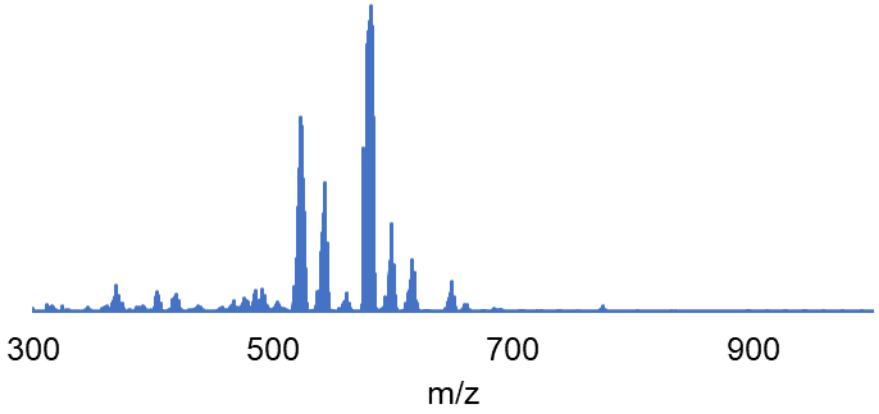

Figure S20. MALDI-TOF mass spectrum of [Ru(Cp)($P^{tBu}_2N^{Ph}_2$)(MeCN)]PF_6 (**1d**) with pyrene as the matrix (1:20 ratio).

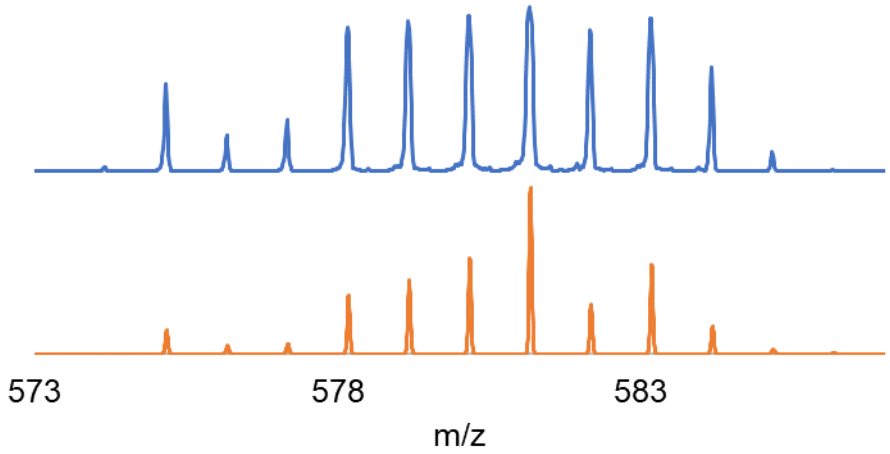

Figure S21. Zoom-in (top) of the observed signal with *m/z* = 581.2 in the MALDI-TOF mass spectrum of [Ru(Cp)($P^{tBu}_2N^{Ph}_2$)(MeCN)]PF_6 (**1d**); and simulation[1] (bottom) of the isotope pattern for the fragment cation [Ru(Cp)($P^{tBu}_2N^{Ph}_2$)]$^+$ with *m/z* = 581.2.

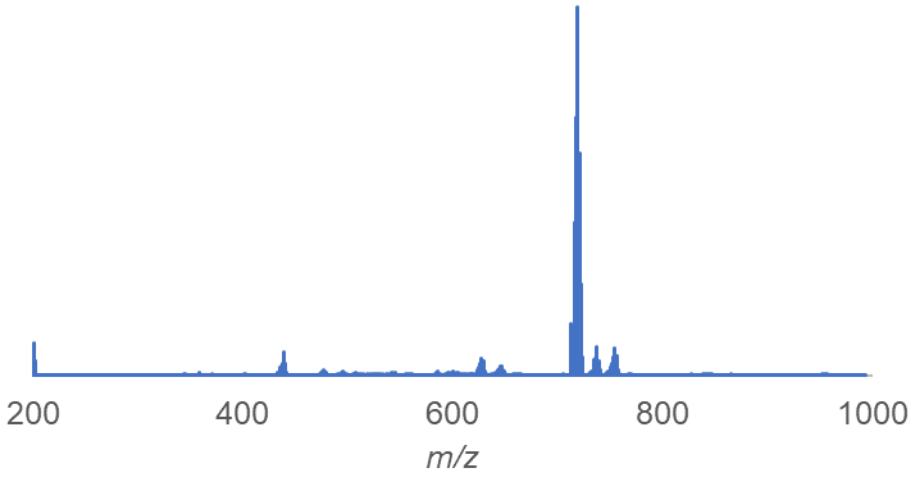

Figure S22. MALDI-TOF mass spectrum of [Ru(Cp*)($P^{Ph}_2N^{Bn}_2$)(MeCN)]PF_6 (**2a**) with pyrene as the matrix (1:20 ratio).

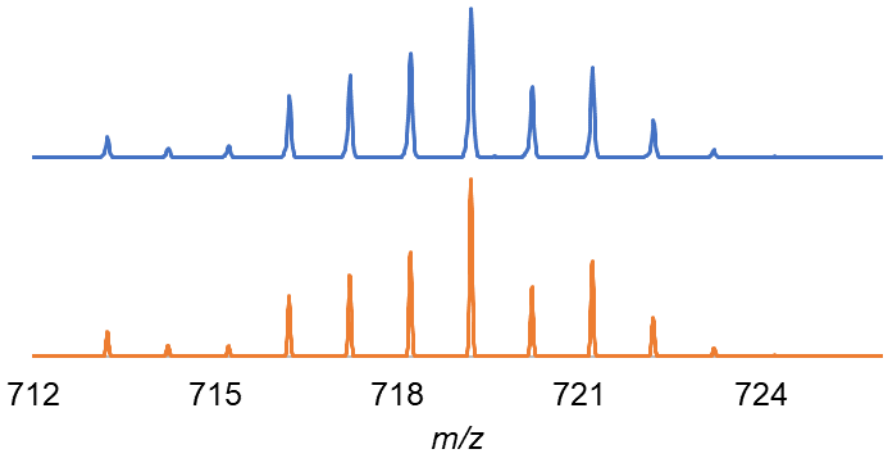

Figure S23. Zoom-in (top) of the observed signal with *m/z* = 719.2 in the MALDI-TOF mass spectrum of [Ru(Cp*)($P^{Ph}_2N^{Bn}_2$)(MeCN)]PF_6 (**2a**); and simulation[1] (bottom) of the isotope pattern for the fragment cation [Ru(Cp*)($P^{Ph}_2N^{Bn}_2$)]$^+$ with *m/z* = 719.2.

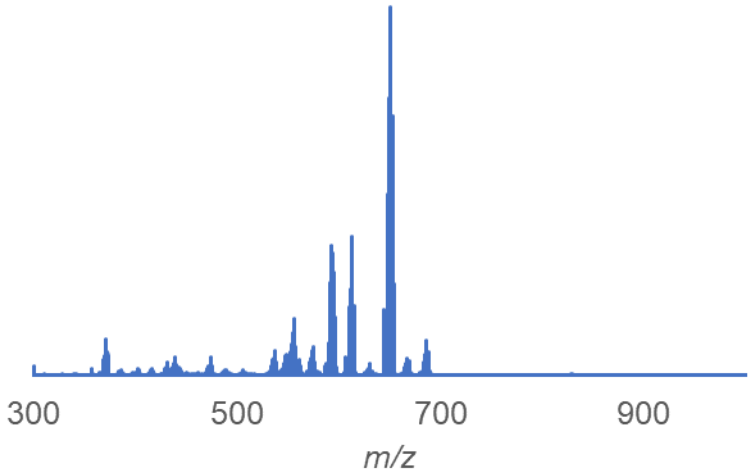

Figure S24. MALDI-TOF mass spectrometry of [Ru(Cp*)($P^{tBu}_2N^{Ph}_2$)(MeCN)]PF_6 (**2d**) with pyrene as the matrix (1:20 ratio).

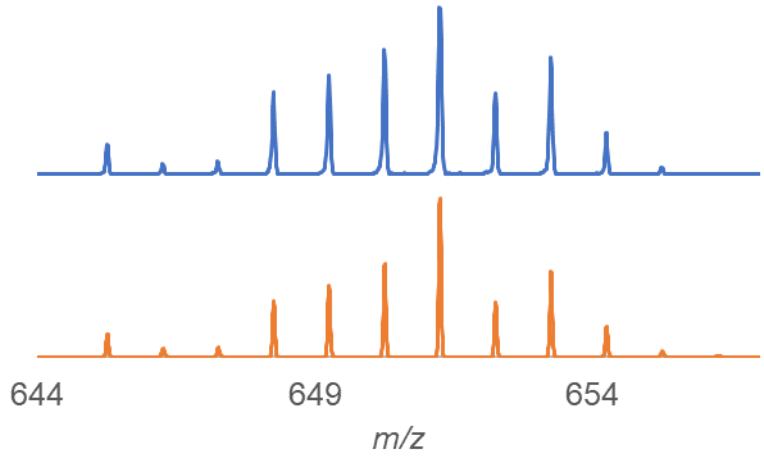

Figure S25. Zoom-in (top) of the observed signal with *m/z* = 651.3 in the MALDI-TOF mass spectrum of [Ru(Cp*)($P^{tBu}_2N^{Ph}_2$)(MeCN)]PF_6 (**2d**); and simulation[1] (bottom) of the isotope pattern for the fragment cation [Ru(Cp*)($P^{tBu}_2N^{Ph}_2$)]$^+$ with *m/z* = 651.3.

IV- Magnetization Transfer Experiments

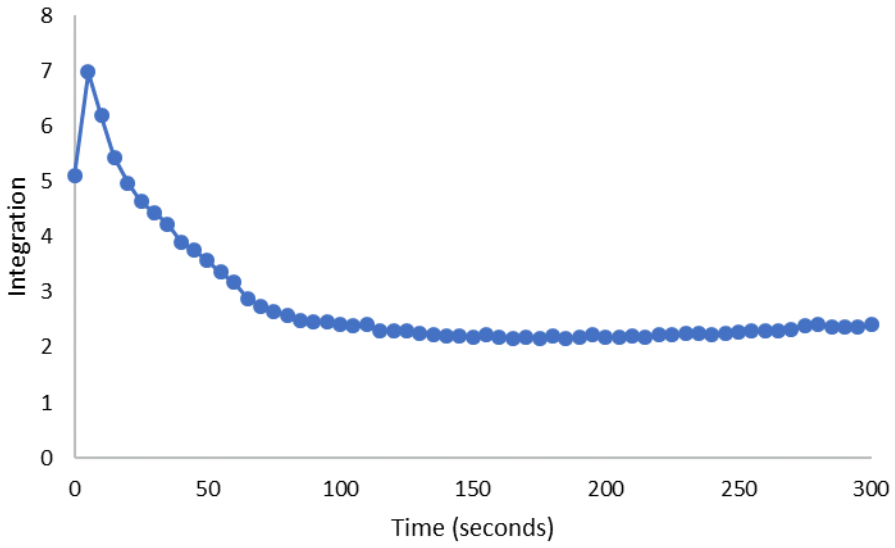

Figure S26. ^{1}H NMR spin-saturation transfer plot; relative integration for bound acetonitrile on [Ru(Cp)($P^{Ph}_2N^{Bn}_2$)(MeCN)]PF_6 (**1a**) after saturating uncoordinated MeCN, as a function of saturation delay time (25 ˚C, CD_2Cl_2).

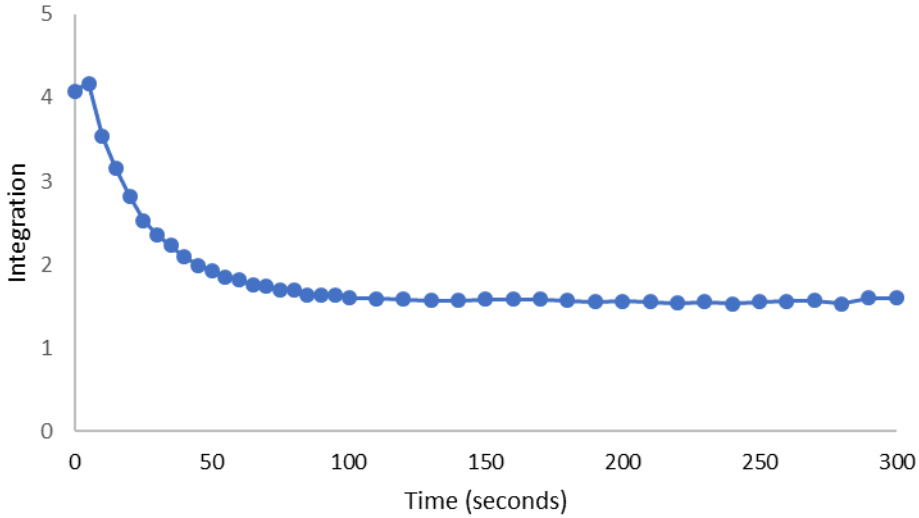

Figure S27. ^{1}H NMR spin-saturation transfer plot; relative integration for bound acetonitrile on [Ru(Cp*)($P^{Ph}_2N^{Bn}_2$)(MeCN)]PF_6 (**2a**) after saturating uncoordinated MeCN, as a function of saturation delay time (25 ˚C, CD_2Cl_2).

V – Catalytic Data

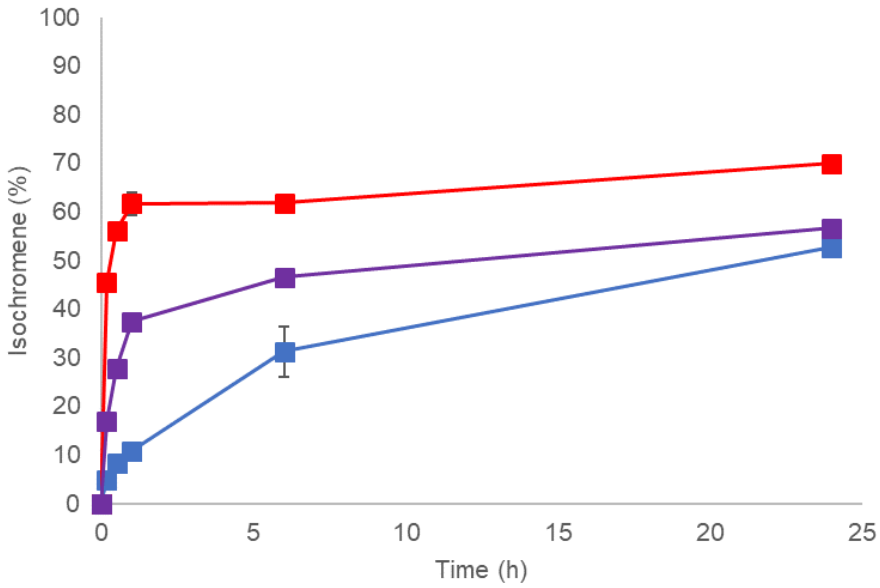

Figure S28. Cyclization of 2-ethynylbenzyl alcohol (150 mM) at 55 ˚C in THF with 0.5 mol% [Ru(Cp)($P^{tBu}_2N^{Ph}_2$)(MeCN)]PF_6 (**1d** – blue), [Ru(Cp*)($P^{Ph}_2N^{Bn}_2$)(MeCN)]PF_6 (**2a** – purple) and [Ru(Cp*)($P^{tBu}_2N^{Ph}_2$)(MeCN)]PF_6 (**2c** – red). Amounts were determined by GC-FID by area count of calibrated signals relative to an internal standard. Reactions were conducted in duplicate. Data points represent the average of the two runs and the error bars give the span of the conversion values of each data set.

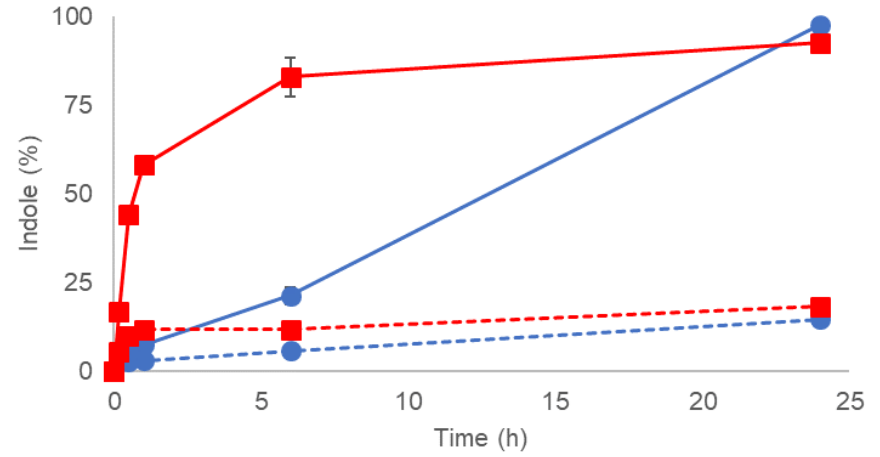

Figure S29. Cyclization of 2-ethynylaniline (150 mM) at 55 ˚C in THF with 0.1 (dashed) and 0.5 (solid) mol% of catalysts [Ru(Cp)($P^{tBu}_2N^{Ph}_2$)(MeCN)]PF_6 (**1d** – blue) and [Ru(Cp*)($P^{tBu}_2N^{Ph}_2$)(MeCN)]PF_6 (**2d** – red). Amounts were determined by GC-FID by area count of calibrated signals relative to an internal standard. Reactions were conducted in duplicate. Data points represent the average of the two runs and the error bars give the span of the conversion values of each data set.

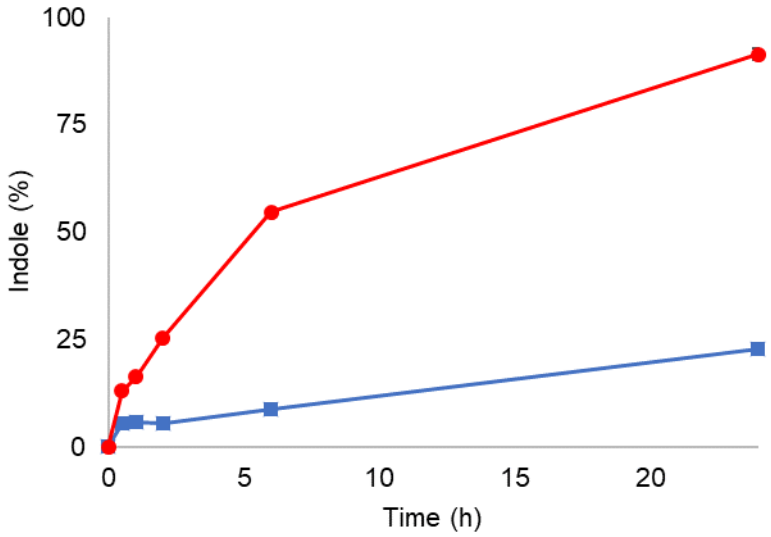

Figure S30. Cyclization of 2-ethynylaniline (150 mM) at 40 ˚C in THF with 0.5 mol% [Ru(Cp)($P^{tBu}_2N^{Ph}_2$)(MeCN)]PF_6 (**1d** – blue) and [Ru(Cp*)($P^{tBu}_2N^{Ph}_2$)(MeCN)]PF_6 (**2d** – red). Amounts were determined by GC-FID by area count of calibrated signals relative to an internal standard. Reactions were conducted in duplicate. Data points represent the average of the two runs and the error bars give the span of the conversion values of each data set.

VI – Crystallographic Details

Data Collection and Processing. The sample of **2d** was mounted on a Mitegen polyimide micromount with a small amount of Paratone N oil. All X-ray measurements were made on a Bruker Kappa Axis Apex2 diffractometer at a temperature of 110 K. The unit cell dimensions were determined from a symmetry constrained fit of 9997 reflections with $5.12° < 2\theta < 60.32°$. The data collection strategy was a number of ω and φ scans which collected data up to 48.5° (2θ). The frame integration was performed using SAINT.[2] The resulting raw data was scaled and absorption corrected using a multi-scan averaging of symmetry equivalent data using SADABS.[3]

Structure Solution and Refinement. The structure for **2d** was solved by using a dual space methodology using the SHELXT program.[4] All non-hydrogen atoms were obtained from the initial solution. The hydrogen atoms were introduced at idealized positions and were allowed to ride on the parent atom. The structural model was fit to the data using full matrix least-squares based on F^2. The calculated structure factors included corrections for anomalous dispersion from the usual tabulation. The structure was refined using the SHELXL program from the SHELXTL suite of crystallographic software.[5] Graphic plots were produced using the SHELXL XP program suite.[6]

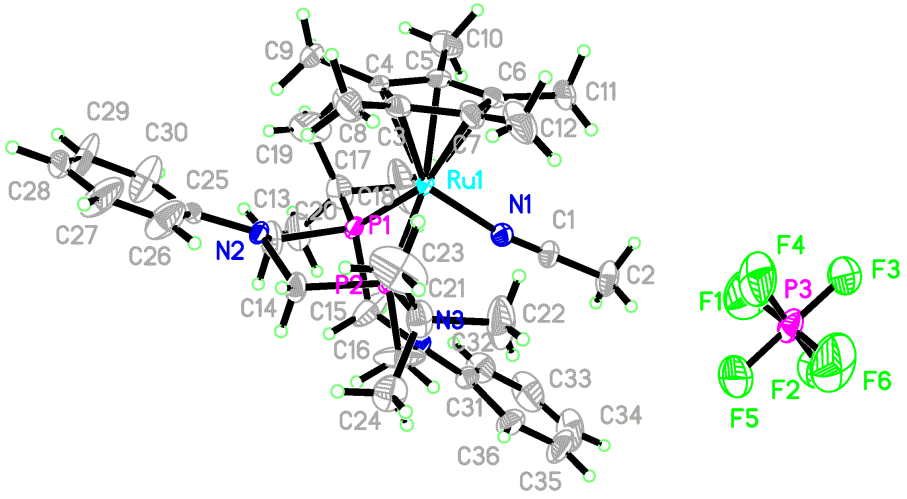

Figure S31. ORTEP drawing of **2d** showing naming and numbering scheme. Ellipsoids are at the 50% probability level and hydrogen atoms were omitted for clarity.

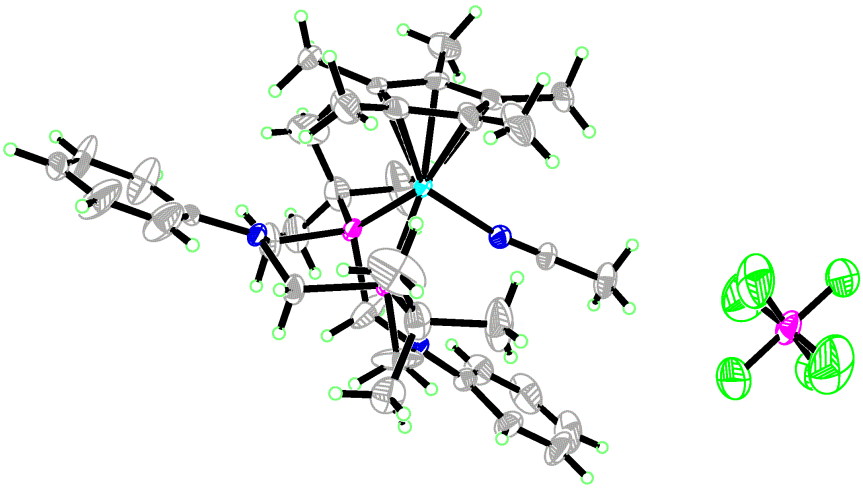

Figure S33. ORTEP drawing of **2d**. Ellipsoids are at the 50% probability level and hydrogen atoms were omitted for clarity.

Table S1. Summary of crystal data for **2d**.

Formula	$C_{36}H_{54}F_6N_3P_3Ru$
CCDC	1891141
Formula Weight (*g/mol*)	836.80
Crystal Dimensions (*mm*)	0.380 × 0.047 × 0.031
Crystal Color and Habit	colourless needle
Crystal System	monoclinic
Space Group	P 2_1/c
Temperature, K	110
a, Å	10.021(5)
b, Å	19.421(9)
c, Å	19.200(10)
α,°	90
β,°	92.243(14)
γ,°	90
V, $Å^3$	3734(3)
Number of reflections to determine final unit cell	9997
Min and Max 2θ for cell determination, °	5.12, 60.32
Z	4
F(000)	1736
ρ (*g/cm*)	1.489
λ, Å, (MoKα)	0.71073
μ, (cm^{-1})	0.609
Diffractometer Type	Bruker Kappa Axis Apex2
Scan Type(s)	*φ* and *ω* scans
Max 2θ for data collection, °	48.5
Measured fraction of data	0.998
Number of reflections measured	65667
Unique reflections measured	6050
R_{merge}	0.0499
Number of reflections included in refinement	6050

Cut off Threshold Expression	$I > 2\sigma(I)$
Structure refined using	full matrix least-squares using F^2
Weighting Scheme	$w=1/[\sigma^2(Fo^2)+(0.0520P)^2+11.8552 P]$ where $P=(Fo^2+2Fc^2)/3$
Number of parameters in least-squares	454
R_1	0.0459
wR_2	0.1138
R_1 (all data)	0.0557
wR_2 (all data)	0.1190
GOF	1.088
Maximum shift/error	0.001
Min & Max peak heights on final ΔF Map (e^-/Å)	-0.833, 0.931

Where:

$R_1 = \Sigma(|F_o| - |F_c|) / \Sigma F_o$

$wR_2 = [\Sigma(w(F_o^2 - F_c^2)^2) / \Sigma(w F_o^4)]^{½}$

GOF = [$\Sigma(w(F_o^2 - F_c^2)^2)$ / (No. of reflns. - No. of params.)]

VII – References

[1] L. Patiny, A. Borel, *J. Chem. Inf. Model.* **2013**, *53*, 1223-1228.

[2] Bruker-Nonius, SAINT, version, 2012.12, **2012**, Bruker-Nonius, Madison, WI 53711, USA

[3] Bruker-Nonius, SADABS, version, 2012.1, **2012**, Bruker-Nonius, Madison, WI 53711, USA.

[4] G. Sheldrick, *Acta Crystallogr. Sect. A* **2015**, *A71*, 3-8.

[5] G. Sheldrick, *Acta Crystallogr. Sect. C* **2015**, *C71*, 3-8.

[6] G. M. Sheldrick, *Acta Crystallogr. Sect. A* **2008**, *A64*, 112-122.